REPORT

SOLID-STATE PHYSICS

Direct determination of mode-projected electron-phonon coupling in the time domain

M. X. Na[1,2]*, A. K. Mills[1,2]*, F. Boschini[1,2], M. Michiardi[1,2,3], B. Nosarzewski[4], R. P. Day[1,2], E. Razzoli[1,2], A. Sheyerman[1,2], M. Schneider[1,2], G. Levy[1,2], S. Zhdanovich[1,2], T. P. Devereaux[4], A. F. Kemper[5], D. J. Jones[1,2]†, A. Damascelli[1,2]†

Ultrafast spectroscopies have become an important tool for elucidating the microscopic description and dynamical properties of quantum materials. In particular, by tracking the dynamics of nonthermal electrons, a material's dominant scattering processes can be revealed. Here, we present a method for extracting the electron-phonon coupling strength in the time domain, using time- and angle-resolved photoemission spectroscopy (TR-ARPES). This method is demonstrated in graphite, where we investigate the dynamics of photoinjected electrons at the $\overline{K}$ point, detecting quantized energy-loss processes that correspond to the emission of strongly coupled optical phonons. We show that the observed characteristic time scale for spectral weight transfer mediated by phonon-scattering processes allows for the direct quantitative extraction of electron-phonon matrix elements for specific modes.

The concept of the electronic quasiparticle as proposed by Landau (*1*) is essential to the modern understanding of condensed matter physics. Among the plethora of interactions relevant to solid-state systems, electron-phonon coupling (EPC)—which is related to phenomena ranging from resistivity in normal metals to conventional [Bardeen-Cooper-Schrieffer (BCS)] superconductivity and charge-ordered phases (*2*, *3*)—has been a persistent subject of interest. Although strong EPC is desirable in systems such as BCS superconductors (*4*, *5*), it is deleterious for conductivity in normal metals, curtailing the application of many compounds as room-temperature electronic devices (*6*).

Given the important role of the electron-phonon interaction in relation to both conventional and quantum materials, extensive theoretical and experimental efforts have been devoted to determining the strength and anisotropy of EPC. Although ab initio calculations are powerful, they rely on complex approximations that require precise experimental data to benchmark their validity (*7*). Inelastic scattering experiments—such as Raman spectroscopy (*8*), electron energy loss spectroscopy (*9*), inelastic x-ray (*10*), and neutron scattering (*11*)—are able to access EPC for specific phonon modes yet are integrated over all electronic states. Angle-resolved photoemission spectroscopy (ARPES), in contrast, can access the strength of EPC via phonon-mediated renormalization effects for specific momentum-resolved electronic states, as revealed by kinks in the electronic band dispersion (*12*–*16*). However, extraction of EPC strength from these kinks requires accurate modeling of the bare band dispersion and of the electronic self-energy, which can prove to be a formidable challenge either because of insufficient sensitivity and experimental resolution (*17*), or because of too-strong and/or compounded many-body interactions (*18*, *19*). In addition, the interpretation of spectroscopic features is often complicated by the fact that they may be attributed to several different many-body interactions (*20*–*22*).

Alternative and possibly more powerful approaches might come from the extension of ARPES into the time domain [time-resolved ARPES (TR-ARPES)], which has already provided deep insights into the relaxation channels of hot electronic distributions, in which EPC plays a major role (*23*–*28*). TR-ARPES performed with 6-eV sources has enabled detailed study of low-energy many-body

[1]Department of Physics and Astronomy, University of British Columbia, Vancouver, BC V6T 1Z1, Canada. [2]Quantum Matter Institute, Vancouver, BC V6T 1Z4, Canada. [3]Max Planck Institute for Chemical Physics of Solids, 01187 Dresden, Germany. [4]Department of Materials Science and Engineering, Stanford Institute for Materials and Energy Sciences, Stanford, CA 94305, USA. [5]Department of Physics, North Carolina State University, Raleigh, NC 27695, USA.
*These authors contributed equally to this work.
†Corresponding author. Email: djjones@physics.ubc.ca (D.J.J.); damascelli@physics.ubc.ca (A.D.)

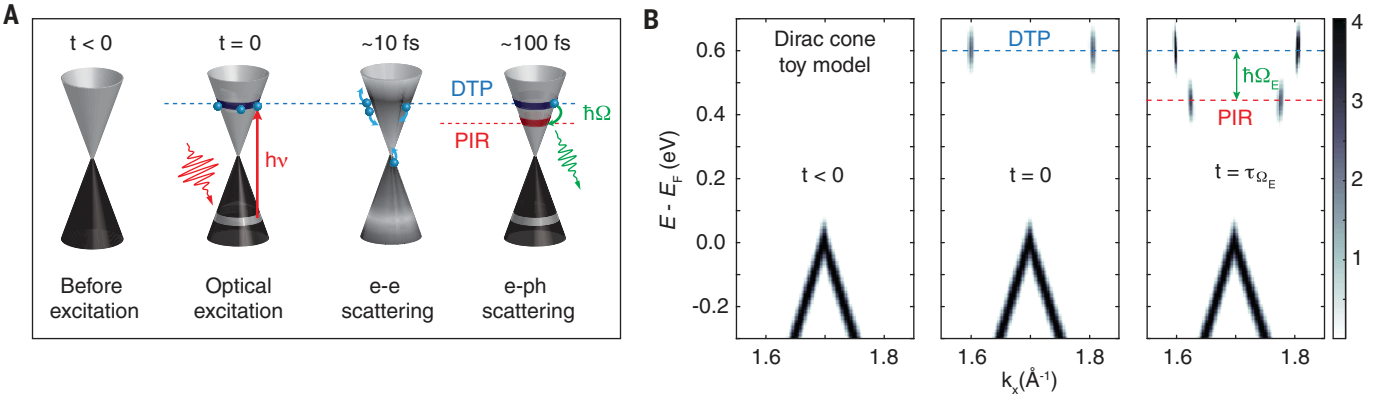

Fig. 1. Toy model of optical injection and scattering processes on the Dirac cone. (**A**) Sketch of the Dirac cone and electron dynamics. Black (gray) indicates occupied (unoccupied) states. During optical excitation, electrons from the lower cone are promoted to the upper cone through a vertical transition (red arrow), creating a direct-transition peak (DTP). Electrons subsequently relax and scatter through electron-electron (e-e) and electron-phonon (e-ph) processes on time scales of 10 and 100 fs, respectively. The former (e-e) broadens the DTP, whereas the latter creates a phonon-induced replica (PIR) by the emission of a phonon. (**B**) Simulation of the transient TR-ARPES intensity for a Dirac cone pumped with 1.2 eV, including a retarded e-ph interaction with a phonon of energy $\hbar\Omega_E$ (*39*). At time t = 0, the DTP feature is observed at $E_{\Omega_E} = 0.6$ eV; at $t = \tau_{\Omega_E}$, the PIR is observed at $E_{DTP} - \hbar\Omega_E$. The intensity of DTP and PIR features is enhanced (×8) for visualization purposes.

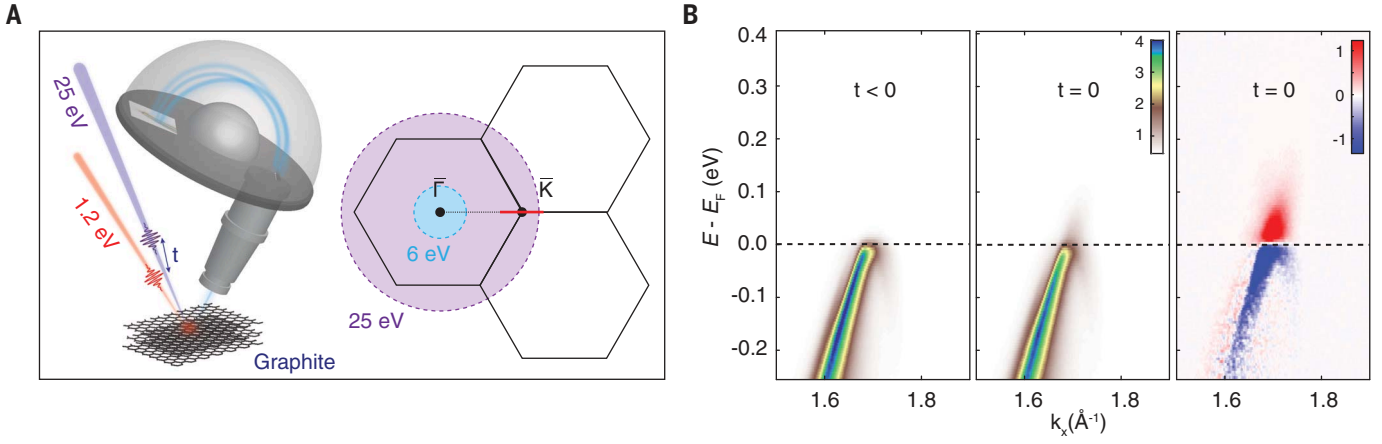

Fig. 2. Electron dynamics measured by TR-ARPES in graphite. (**A**) The experimental setup, along with the 2D-projected Brillouin zone of graphite. Blue (purple) circle indicates the range of momenta accessible to 6-eV (25-eV) photons. We measure along the $\overline{\Gamma} - \overline{K}$ direction, cut shown in red. (**B**) TR-ARPES measurements acquired with a 25-eV probe and 1.19-eV pump. Sample temperature is 50 K before pump arrival. The unpumped dispersion ($t < 0$) is shown in the left panel. The pumped ARPES map at zero delay and the differential map are shown in the middle and right panels, respectively. Owing to fast thermalization processes, the signal of DTP and PIR cannot be observed by simple visual inspection on a linear colormap.

phenomena; although this has provided a fresh perspective on superconducting gap dynamics of cuprate superconductors (*29*–*31*), electron-phonon interaction in bulk FeSe (*32*), and surface-state dynamics in topological materials (*26*, *33*), low photon energies have limited these studies to a small region of the Brillouin zone (BZ). ARPES systems using high-harmonic sources have extended the accessible momenta beyond the first BZ, but heretofore they have focused on the high-energy–scale electron dynamics on the order of 10 fs (*25*, *27*, *34*, *35*), as energy resolutions have yet to reach the standards achieved by 6-eV systems.

Here, we explore a paradigm for the TR-ARPES study of transient spectral features at large momenta, made possible by a femtosecond high-harmonic source designed with specific emphasis on energy resolution (*36*). The experimental strategy is as follows: We begin by injecting electrons into specific unoccupied states by optical excitation. As the hot electrons relax, we track specifically the transfer of spectral weight from these photoexcited states to lower-energy states via emission of a phonon with energy $\hbar\Omega_{\mathbf{q},\nu}$, where $\mathbf{q}$ and ν denote the phonon momentum and branch, respectively. The time constant extracted for this transfer of spectral weight ($\tau_{\mathbf{q},\nu}$) can then be directly related to the electron-phonon contribution to the self-energy for the phonon involved as

$$\frac{1}{\tau_{\mathbf{q},\nu}} = \frac{2\pi}{\hbar}\langle g^2_{\mathbf{q},\nu}\rangle D(E - \hbar\Omega_{\mathbf{q},\nu}) \qquad (1)$$

where $\hbar$ is the reduced Planck constant, E is the energy of the direct optical transition, $\langle g^2_{\mathbf{q},\nu}\rangle$ is the square of the mode-projected electron-phonon matrix element averaged over the states populated by optical excitation, and $D(E)$ is the electronic density of states (DOS) (*7*, *37*, *38*) [for derivation, see (*39*)]. Below, we show that this allows us to measure $\langle g^2_{\mathbf{q},\nu}\rangle$, gaining insight on the strength of the scattering process as well as the energy and momenta involved.

To track the transfer of spectral weight, the initial (photoinjected) states and final states must be unambiguously defined and located. This is easiest on a small Fermi surface, such as that of graphene, where phase-space scattering restrictions limit the number of initial and final states. To visualize the aforementioned electron-phonon scattering process, we simulate the pump-probe experiment using a Dirac dispersion as a toy model and calculate the transient ARPES spectra in response to optical excitation for the case of a single strongly coupled Einstein phonon mode of energy $\hbar\Omega_{\mathbf{q},\nu} = \hbar\Omega_E$. This model (Fig. 1B) uses a two-time Green's function formalism on the Keldysh contour for a multiorbital system. At $t = 0$, the system is excited with a 1.2-eV pulse, which promotes electrons via direct optical excitation to 0.6 eV, observed experimentally as the direct-transition peak (DTP). Then, on the characteristic time scale of $\tau_{\mathbf{q},\nu} = \tau_{\Omega_E}$, the electron-phonon interaction leads to relaxation of the photoinjected electron population via the emission of phonons, resulting in the creation of a phonon-induced replica (PIR) at an energy $E_{PIR} = 0.6\ \text{eV} - \hbar\Omega_E$. In contrast to the toy model, other scattering processes (such as electron-electron scattering) compete with this electron-phonon scattering process in the actual experiment, resulting in a smaller PIR and a larger background. In comparing Fig. 1B and Fig. 2B, we do not see the predicted DTP and PIR features in the intensity map. However, we show that these features are plainly visible in the momentum-integrated energy distribution curves (Fig. 3).

In this study, we perform the experiment on graphite, which has the same ideal phase-space restrictions as its monolayer counterpart but does not require consideration of substrate coupling, which in graphene is known to affect both electronic and phononic structure, as well as EPC (*40*–*42*). The low-energy electronic structure of single-crystal graphite consists of two gapless, nearly two-dimensional (2D) Dirac-like bands at the BZ corners (similar to graphene) as well as a second set of bands that disperse along the c axis ($k_\perp$ in our experimental geometry, see Fig. 4A) (*43*–*45*). In addition, graphite electrons are well known to couple to optical phonons at $\overline{\Gamma}$ and $\overline{K}$ (*10*, *46*–*50*) and have been extensively studied both theoretically and experimentally (*8*, *24*, *28*), making graphite an ideal benchmark system for the application of this time-resolved technique.

Previous time-resolved experiments have shown that the time (energy) scale of the electron-phonon scattering process is on the order of 100 fs (100 meV). Therefore, observation of this transient spectral signature in TR-ARPES demands a balance of time and energy resolution. Achieving the system resolution requirements at photon energies needed to reach the $\overline{K}$ point (>20 eV, assuming a maximum detection angle of 60°; see Fig. 2A for the BZ range covered by photons of different energy) was made

viable by the development of a new cavity-based high-harmonic source (*36*). We select the 21st harmonic (25 eV) from the high-harmonic spectrum for photoemission, with an overall time (energy) resolution of 190 fs (22 meV) and a repetition rate of 60 MHz. The unpumped ARPES map of the Dirac-like dispersion along $\overline{\Gamma}-\overline{K}$ is shown in the left panel of Fig. 2B, where only one branch of the cone is observed as a consequence of photoemission matrix elements (*51*, *52*). In the middle and right panels of Fig. 2B, we show, respectively, the pumped ARPES spectra at zero delay and the differential map (obtained by subtracting the equilibrium map from the map at zero pump-probe delay). The data were measured under perturbative excitation by a 1.19-eV pump pulse with an incident fluence of 18 μJ/cm^2, where red (blue) color indicates a transient increase (decrease) of photoemission intensity. The time scales of the anticipated primary scattering processes after optical excitation are sketched in Fig. 1A. After the creation of the DTP above the Fermi level (E_F), electrons decay into a thermal distribution, mainly via electron-electron (e-e) and electron-phonon (e-ph) scattering events. Because the e-e scattering processes are about an order of magnitude faster than e-ph scattering (*53*), we should observe a rapid buildup of photoemission intensity at the Fermi energy. This can render the observation of the DTP and PIR nontrivial, requiring a careful analysis of features above the hot-electron background.

In Fig. 3A, we display the momentum-integrated energy distribution curve ($\int$EDC $d\mathbf{k}$) along the $\overline{\Gamma}-\overline{K}$ direction (open circles). We stress that the $\int$EDC $d\mathbf{k}$ is proportional to the occupied DOS along the selected momentum cut shown in Fig. 2A (*39*). Filled circles in Fig. 3A represent the $\int$EDC $d\mathbf{k}$ after removal of a biexponential background given by the thermal electronic distribution (near E_F) and nonthermal e-e scattering processes (near 0.6 eV) (*39*). Once this background is removed, the $\int$EDC $d\mathbf{k}$ directly exposes the transient peaks, which can be fitted with five Lorentzians of the same width (Fig. 3A). We can immediately identify the prominent peak at 0.6 eV as DTP$_1$, which was anticipated in the toy model (Fig. 1B) and is associated with the optical transition from the π_2-to-π_3 band in Fig. 4A. The other peaks—as we show in more detail below—are a combination of PIRs and other DTPs, which arise from the second set of electronic bands (π_1, π_4) that disperse in $k_\perp$. We confirm these transitions in Fig. 4A with a calculation of the optical joint DOS for graphite (*54*), adapted from a tight-binding model in (*45*), for a pump photon energy of 1.19 eV. The possible transitions along the $\overline{\Gamma}-\overline{K}$ cut are shown in Fig. 4A. Whereas the π_2-to-π_4 transition is outside the range of our data, the three lower DTPs fall exactly in the energy range we expect. The resulting momentum-integrated optical joint DOS is shown in Fig. 4B, along with the energy position of the five fitted peaks from Fig. 3A.

To illustrate the DTP-to-PIR scattering process, we focus on the time evolution of the three most prominent peaks, shown in Fig. 3B; for a discussion of the DTP$_2$-PIR$_2$ pair, see (*39*). The combined time and energy resolution of our source allows for a detailed study of the transient evolution of the DTP and the PIR, given by the amplitude of the Lorentzians in Fig. 3C. Despite being only 50 meV apart, the dynamics of the light-blue and red peaks are markedly different. The population of the light-blue peak is only slightly delayed with respect to the dark-blue DTP$_1$ and is identified with a direct optical excitation (π_1-to-π_4 band in Fig. 4A, labeled DTP$_2$), with the temporal delay being a consequence of energy-dependent electron lifetime (*55*, *56*). In contrast, the population of the red peak is delayed by $\Delta t = 47 \pm 9$ fs, too large to be compatible with optical excitation. This population instead corresponds to the simulated PIR in Fig. 1B, where the energy of the phonon involved is $\hbar\Omega_{\mathbf{q},\nu} = E_{DTP} - E_{PIR} = 0.165 \pm 0.011$ eV.

The solid curves in Fig. 3C are the result of a phenomenological rate-equation model describing the transfer of spectral weight between the DTP and the PIR pairs (*39*). The population of electrons in the (dark and light) blue DTP are governed by rate equations involving three terms: population by a 120-fs pump pulse, energy-dependent thermalization of the excited state population to the hot-electron bath (τ_{th}), and energy-dependent phonon-mediated decay of the excited state

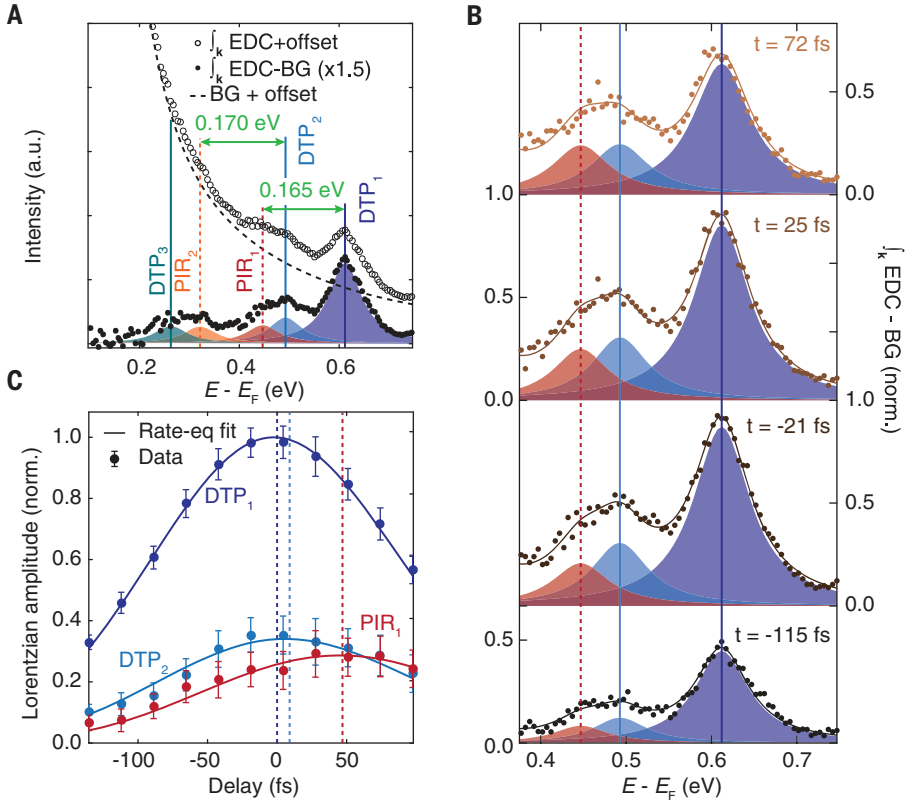

Fig. 3. Time dependence of photoinduced excitations in graphite. Sample temperature is 50 K before pump arrival. (**A**) Open circles display the momentum-integrated energy distribution curve $\int$EDC $d\mathbf{k}$, where signal is integrated in momentum along the $\overline{\Gamma}-\overline{K}$ direction. The subtraction of the biexponential hot-electron background (BG) highlights a series of peaks (filled circles), which are a combination of DTPs and PIRs. Solid (dashed) lines indicate the fitted position of DTP (PIR) peaks. The phonon energies extracted between the DTP$_1$-PIR$_1$ and DTP$_2$-PIR$_2$ pairs are 0.165 eV and 0.170 eV, respectively, as indicated by the green arrows. (**B**) Evolution of the most prominent peaks. Dark (light) blue corresponds to DTP$_1$ (DTP$_2$), red corresponds to PIR$_1$. The amplitudes are indicative of the population of electrons in each state. (**C**) The Lorentzian amplitude for each peak shown in (B) is plotted as a function of time. Dashed lines indicate the peak delay: DTP$_2$ (PIR$_1$) is delayed 9 fs (47 fs) with respect to DTP$_1$. Solid curves indicate the electronic occupation for the specified states derived from the rate-equation model fit. The transfer of spectral weight from DTP$_1$ to PIR$_1$ is associated to an e-ph scattering time constant $\tau_{\mathbf{q},\nu} = 174 \pm 35$ fs.

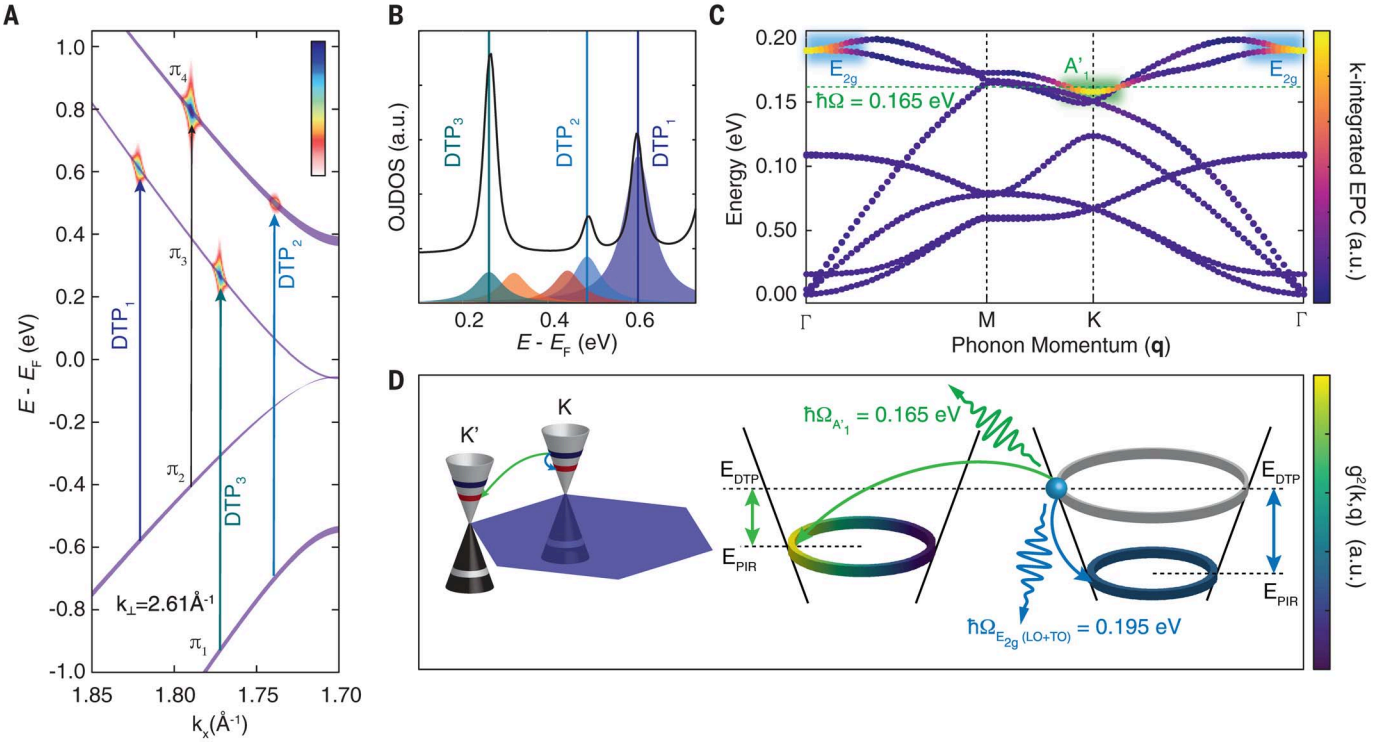

Fig. 4. Calculation of the optical joint DOS and e-ph coupling. (**A**) Momentum-resolved optical joint DOS, extracted using a modified tight-binding model from (*39*, *45*, *54*), showing the available optical transitions between the bands of graphite for a pump photon energy of 1.19 eV, integrated around $k_\perp = 2.61\text{Å}^{-1}$. This value is fitted using an inner potential of $V_0 = 16.4 \pm 0.1$ eV (*44*). (**B**) Integrated optical joint DOS (OJDOS) along the $\overline{\Gamma} - \overline{\text{K}}$ direction. The peaks extracted from Fig. 3A are also shown, with the location of the fitted DTP overlaid in solid lines, displaying good agreement with the optical joint DOS. (**C**) The phonon-dispersion of graphite as calculated from DFT (*38*). Colors represent the strength of the total EPC (i.e., integrated over all electronic momenta) (*39*). The dominant mode A'_1 (E_{2g}) is highlighted in green (blue) (*46*). (**D**) Calculation of the $\langle g^2_{\mathbf{k},\mathbf{q}} \rangle$ (*39*). Case one: electron scattering with an A'_1 mode (green) with momentum ~K from a specific state (indicated by the blue sphere) in the 0.61-eV energy contour at K to states in the 0.45-eV contour at K′. Case two: electron scattering with an E_{2g} (blue) mode with momentum ~0 from a specific state in the 0.61-eV energy contour at K to states in the 0.41-eV contour at K. $\langle g^2_{A'_1} \rangle$ and $\langle g^2_{E_{2g}} \rangle$ are obtained by integrating over both the constant energy contour at E_{PIR} and the electron position along the contour at E_{DTP}. Colors indicate that the value of $\langle g^2_{A'_1} \rangle$ is twice that of the LO and TO combined $\langle g^2_{E_{2g}} \rangle$ (see text for precise values). The scattering process from K′ to K (not shown) is identical.

population ($\tau_{\mathbf{q},\nu}$). This latter term transfers spectral weight from the DTP$_i$ to the PIR$_i$, which lose electrons to the same thermalization and phonon-mediated decay terms. The resultant temporal evolution is then convolved with a Gaussian with a full width at half maximum of 150 fs to account for the pulse duration of the photoemission probe. With this simple model, we find that a thermalization constant of $\tau_{\text{th}} = 56 \pm 16$ fs and an e-ph decay constant of $\tau_{\mathbf{q},\nu} = 174 \pm 35$ fs reproduce well the delay and relative population of the nonthermal signatures. In addition, the extracted $\tau_{\mathbf{q},\nu}$ is consistent with ab initio calculations and estimates for e-ph scattering time in previous time-resolved studies (*25*, *27*, *28*, *53*, *57*). Because we are coupling to a single-phonon mode of energy $\hbar\Omega_{\mathbf{q},\nu} = 0.165 \pm 0.011$ eV, we can directly relate this time constant to the mode-projected e-ph matrix element via Eq. 1, using an electronic DOS $[D(E - \hbar\Omega_{\mathbf{q},\nu}) = 0.0241\,\text{eV}^{-1}]$ calculated from the tight-binding model in Fig. 4A. From this, we obtain a value of $\langle g^2_{\mathbf{q},\nu} \rangle = 0.050 \pm 0.011\,\text{eV}^2$.

We now assign the observed PIR to scattering by a specific phonon mode by comparing the extracted $\hbar\Omega_{\mathbf{q},\nu}$ against the phonon dispersion of graphite calculated by density functional theory (DFT) in Fig. 4C. The colors represent the EPC integrated over all electronic momenta and indicate strong coupling for the E_{2g} mode at Γ and the A'_1 mode at K. The latter is the phonon mode associated with the DTP-PIR pair we observe, as its energy matches the 0.165 eV we extract (green dashed line). Given that it has momentum K, this mode is associated with the intervalley scattering of electrons between states at $\overline{\text{K}}$ and $\overline{\text{K}'}$. We consider this scattering process explicitly for a single electron in Fig. 4D (green arrow). Starting from an initial state i on the constant energy contour E_{DTP_1}, we calculate the matrix element $g^2_{\mathbf{k},\mathbf{q}}$ for scattering events leading to the final state f on the constant energy contour $E_{\text{DTP}_1} - \hbar\Omega_{A'_1}$, such that $\mathbf{k}_f - \mathbf{k}_i = \mathbf{q}$ is fulfilled. This mode-projected calculation gives a value of $\langle g^2_{A'_1} \rangle = 0.040\,\text{eV}^2$, in agreement with the experimental value of $\langle g^2_{\mathbf{q},\nu} \rangle = \langle g^2_{A'_1} \rangle = 0.050 \pm 0.011\,\text{eV}^2$ that we previously extracted from the rate-equation fits to the experimental data. In addition to the A'_1 mode, Fig. 4C suggests that the Γ – E_{2g} modes [longitudinal (LO) and transverse (TO) modes] are also expected to be strongly coupled; however, considering the scattering process as before, we extract for the degenerate LO and TO modes a total coupling $\langle g^2_{E_{2g}} \rangle = 0.023\,\text{eV}^2$, which corresponds to a time constant of >300 fs. This coupling is ~50% that of the A'_1 mode, which is consistent with previous theoretical considerations (*58*). Thus, the PIR associated with emission of the

$\Gamma - E_{2g}$ phonons would not be visible above the hot-electron background in our experiment.

In this work, we have shown a proof-of-principle extraction of the mode-projected e-ph matrix element $\langle g^2_{A'_1} \rangle$ in graphite. We remark that $\langle g^2 \rangle$ is a fundamental quantity, defined as the momentum average of the change in the electronic Hamiltonian in response to the ionic displacements of a phonon (eq. S13). In particular, $\langle g^2 \rangle$ is independent of doping and specified for a well-defined set of initial and final electronic states and a well-defined bosonic mode (in this case, the A'_1 optical phonon with momentum K in graphite). Nonetheless, it is instructive to estimate the EPC constant $\lambda = 2\langle g^2 \rangle D(E_F)/(\hbar\Omega)$ for comparison with other approaches (*7*). Commonly seen in relation to the critical temperature in superconductivity, the quantity λ is doping-dependent and integrated over all bosonic and electronic degrees of freedom. Therefore, caution must be applied in comparing the two quantities. In pristine and low-doping graphene or graphite systems, the vanishing DOS at the Dirac point of graphene (crossing point of graphite) makes extraction of λ very difficult, with reported values ranging from 4×10^{-4} to 1.1 (*20*, *47*, *59*–*63*), while DFT predicts $\lambda < 0.05$ (*17*). Even forgoing doping dependence, the large range of reported λ values clearly illustrates the difficulty ARPES has in extracting the EPC of this particular system. In this work, we extract $\langle g^2_{A'_1} \rangle$ for the DTP state at 0.6 eV, corresponding to a value of the mode-projected EPC $\lambda_{A'_1} = 0.0182 \pm 0.004$. This value characterizes a system where the Fermi level is doped up to 0.6 eV above the crossing point (the value at zero doping would be $\lambda_{A'_1} = 0.006 \pm 0.001$). We would ideally compare this value with that extracted by kink analysis in graphite, but the strong curvature of the bare-band dispersion (*61*) and the lack of studies at comparable doping make this particularly challenging. Thus, we instead compare this value to what is reported in (*20*), a doping-dependent study of λ in graphene that is additionally supported by DFT calculations (*17*). When the system is doped such that the Dirac point is 0.6 eV below E_F (corresponding to a carrier density of $n \approx 4 \times 10^{13}$ cm^{-2}), then $\lambda \approx 0.035$ is extracted. From this, we see that $\lambda_{A'_1} \approx \lambda/2$, which is consistent with the fact that $\lambda_{A'_1}$ captures only one of two strongly coupled modes in the system (the other being E_{2g}), whereas λ as extracted from kink analysis is integrated over all modes. Together, these results suggest that time-domain measurements have the ability to access the EPC in a precise, sensitive, and mode-projected way.

In principle, this technique is applicable to materials in which electrons are sufficiently strongly coupled to one or a few bosonic modes, such that distinct boson-induced replicas can be observed. Beyond graphite and graphene, quasi-2D materials such as transition-metal dichalcogenides feature gapped bands at the K and K′ points, with further restrictions of the phase space for scattering stemming from valley degrees of freedom, and would be ideal candidates for similar TR-ARPES studies. In addition, conventional and unconventional superconductors, such as MgB_2 or cuprate- or Fe-based superconductors, respectively, famously feature strong coupling to bosonic modes, which may drive electronic renormalizations (kinks). By monitoring quantized decay processes across the full BZ, this nonequilibrium technique will offer a distinct approach for studying the microscopic origin and momentum dependence of electron-boson coupling and its role in the emergence of superconductivity.

These results also prove that a fresh analytical perspective can be achieved in TR-ARPES by taking advantage of femtosecond sources that combine high photon energy (to access large electronic momenta) with high-energy resolution (to resolve the low-energy quasiparticle dynamics). With the development of tunable pumps, polarization control for pump and probe, and bandwidth control to balance the trade-off between energy and time resolution, a growing versatility will be available for TR-ARPES experiments. By monitoring the population of electrons injected into momentum- and energy-selected states by direct optical excitation, it would be possible to formulate a series of studies on empty state dispersion, lifetime, decoherence, and electron-boson interactions in a wide range of quantum materials.

REFERENCES AND NOTES

1. L. D. Landau, *J. Exp. Theor. Phys.* **3**, 920 (1957).
2. M. Le Tacon *et al.*, *Nat. Phys.* **10**, 52–58 (2014).
3. T. P. Devereaux *et al.*, *Phys. Rev. X* **6**, 041019 (2016).
4. M. Strongin *et al.*, *Phys. Rev. Lett.* **21**, 1320–1323 (1968).
5. W. L. McMillan, *Phys. Rev.* **167**, 331–344 (1968).
6. M. Scheuch *et al.*, *Appl. Phys. Lett.* **99**, 211908 (2011).
7. F. Marsiglio, J. P. Carbotte, in *Superconductivity: Conventional and Unconventional Superconductors*, K. H. Bennemann, J. B. Ketterson, Eds. (Springer-Verlag, 2008), pp. 73–162.
8. A. C. Ferrari, *Solid State Commun.* **143**, 47–57 (2007).
9. S.-i. Tanaka, K. Mukai, J. Yoshinobu, *Phys. Rev. B* **95**, 165408 (2017).
10. M. Mohr *et al.*, *Phys. Rev. B* **76**, 035439 (2007).
11. T. Yildirim *et al.*, *Phys. Rev. Lett.* **87**, 037001 (2001).
12. T. Valla, A. V. Fedorov, P. D. Johnson, S. L. Hulbert, *Phys. Rev. Lett.* **83**, 2085–2088 (1999).
13. S. LaShell, E. Jensen, T. Balasubramanian, *Phys. Rev. B* **61**, 2371–2374 (2000).
14. A. Lanzara *et al.*, *Nature* **412**, 510–514 (2001).
15. A. Damascelli, *Phys. Scr.* **2004**, 61 (2004).
16. J. Shi *et al.*, *Phys. Rev. Lett.* **92**, 186401 (2004).
17. M. Calandra, F. Mauri, *Phys. Rev. B* **76**, 205411 (2007).
18. N. J. Ingle *et al.*, *Phys. Rev. B* **72**, 205114 (2005).
19. C. N. Veenstra, G. L. Goodvin, M. Berciu, A. Damascelli, *Phys. Rev. B* **84**, 085126 (2011).
20. D. A. Siegel, C. Hwang, A. V. Fedorov, A. Lanzara, *New J. Phys.* **14**, 095006 (2012).
21. C. Zhang *et al.*, *Nat. Commun.* **8**, 14468 (2017).
22. F. Li, G. A. Sawatzky, *Phys. Rev. Lett.* **120**, 237001 (2018).
23. L. Perfetti *et al.*, *New J. Phys.* **10**, 053019 (2008).
24. Y. Ishida *et al.*, *Sci. Rep.* **1**, 64 (2011).
25. I. Gierz *et al.*, *Nat. Mater.* **12**, 1119–1124 (2013).
26. J. A. Sobota *et al.*, *J. Electron Spectrosc. Relat. Phenomena* **195**, 249–257 (2014).
27. A. Stange *et al.*, *Phys. Rev. B* **92**, 184303 (2015).
28. J. A. Yang, S. Parham, D. Dessau, D. Reznik, *Sci. Rep.* **7**, 40876 (2017).
29. L. Perfetti *et al.*, *Phys. Rev. Lett.* **99**, 197001 (2007).
30. C. L. Smallwood *et al.*, *Science* **336**, 1137–1139 (2012).
31. F. Boschini *et al.*, *Nat. Mater.* **17**, 416–420 (2018).
32. S. Gerber *et al.*, *Science* **357**, 71–75 (2017).
33. J. A. Sobota *et al.*, *Phys. Rev. Lett.* **108**, 117403 (2012).
34. T. Rohwer *et al.*, *Nature* **471**, 490–493 (2011).
35. F. Cilento *et al.*, *Sci. Adv.* **4**, eaar1998 (2018).
36. A. K. Mills *et al.*, *Rev. Sci. Instrum.* **90**, 083001 (2019).
37. M. Sentef *et al.*, *Phys. Rev. X* **3**, 041033 (2013).
38. T. Sohier, thesis, De L'Université Pierre et Marie Curie Spécialité, Paris, France (2016).
39. Materials and methods are available as supplementary materials.
40. S. Y. Zhou *et al.*, *Nat. Mater.* **6**, 770–775 (2007).
41. Y. Y. Wang *et al.*, *J. Phys. Chem. C* **112**, 10637–10640 (2008).
42. A. Allard, L. Wirtz, *Nano Lett.* **10**, 4335–4340 (2010).
43. J. C. Slonczewski, P. R. Weiss, *Phys. Rev.* **109**, 272–279 (1958).
44. A. Grüneis *et al.*, *Phys. Rev. Lett.* **100**, 037601 (2008).
45. C. M. Cheng *et al.*, *Appl. Surf. Sci.* **354**, 229–234 (2015).
46. S. Piscanec, M. Lazzeri, F. Mauri, A. C. Ferrari, J. Robertson, *Phys. Rev. Lett.* **93**, 185503 (2004).
47. S. Y. Zhou, G. H. Gweon, A. Lanzara, *Ann. Phys.* **321**, 1730–1746 (2006).
48. M. Lazzeri, C. Attaccalite, L. Wirtz, F. Mauri, *Phys. Rev. B* **78**, 081406 (2008).
49. R. P. Chatelain, V. R. Morrison, B. L. M. Klarenaar, B. J. Siwick, *Phys. Rev. Lett.* **113**, 235502 (2014).
50. M. J. Stern *et al.*, *Phys. Rev. B* **97**, 165416 (2018).
51. I. Gierz, J. Henk, H. Höchst, C. R. Ast, K. Kern, *Phys. Rev. B* **83**, 121408(R) (2011).
52. Y. Liu, G. Bian, T. Miller, T. C. Chiang, *Phys. Rev. Lett.* **107**, 166803 (2011).
53. S. Ulstrup *et al.*, *J. Phys. Condens. Matter* **27**, 164206 (2015).
54. R. P. Day, B. Zwartsenberg, I. S. Elfimov, A. Damascelli, *NPJ Quant. Mat.* **4**, 54 (2019).
55. S. Xu *et al.*, *Phys. Rev. Lett.* **76**, 483–486 (1996).
56. P. Narang, L. Zhao, S. Claybrook, R. Sundararaman, *Adv. Opt. Mater.* **5**, 1600914 (2017).
57. J. C. Johannsen *et al.*, *Phys. Rev. Lett.* **111**, 027403 (2013).
58. S. Butscher, F. Milde, M. Hirtschulz, E. Malić, A. Knorr, *Appl. Phys. Lett.* **91**, 203103 (2007).
59. K. Sugawara, T. Sato, S. Souma, T. Takahashi, H. Suematsu, *Phys. Rev. Lett.* **98**, 036801 (2007).
60. A. Bostwick, T. Ohta, T. Seyller, K. Horn, E. Rotenberg, *Nat. Phys.* **3**, 36–40 (2007).
61. C. S. Leem *et al.*, *Phys. Rev. Lett.* **100**, 016802 (2008).
62. S. Ulstrup *et al.*, *Phys. Rev. B* **86**, 161402(R) (2012).
63. F. Joucken *et al.*, *Phys. Rev. B* **93**, 241101(R) (2016).
64. M. Na, Replication Data for: Direct determination of mode-projected electron-phonon coupling in the time-domain, Version 1, Harvard Dataverse (2019); https://doi.org/10.7910/DVN/TFKS8Z.
65. M. Na, mengxing-n/graphite: v1.0.0, Version 1, Zenodo (2019); https://doi.org/10.5281/zenodo.3525476.

ACKNOWLEDGMENTS

We gratefully acknowledge M. Berciu, G. A. Sawatzky, A. Nocera, Z. Ye, and D. Manske for critical reading of the manuscript and useful discussions, as well as C. Gutierréz for guidance on figure presentation. **Funding:** This research was undertaken thanks in part to funding from the Max Planck-UBC-UTokyo Centre for Quantum Materials and the Canada First Research Excellence Fund, Quantum Materials and Future Technologies Program. This project is funded in part by the Gordon and Betty Moore Foundation's EPiQS Initiative, Grant GBMF4779 to A.D. and D.J.J.; the Killam, Alfred P. Sloan, and Natural Sciences and Engineering Research Council of Canada's (NSERC's) Steacie Memorial Fellowships (A.D.); the Alexander von Humboldt Fellowship (A.D.); the Canada Research Chairs Program (A.D.); NSERC, Canada Foundation for Innovation (CFI); British Columbia Knowledge Development Fund (BCKDF); and the CIFAR Quantum Materials Program. E.R. acknowledges support from the Swiss National Science Foundation (SNSF) grant P300P2_164649. A.F.K. acknowledges support by the National Science Foundation under grant DMR-1752713. B.N. and T.P.D. acknowledge funding from the Department of Energy, Basic Energy Sciences, Division of Materials Science. **Author contributions:** This study was conceived of by M.X.N., A.K.M., F.B., M.M., D.J.J., and A.D.; and

the experiment was carried out by M.X.N., A.K.M., F.B., and M.M., with experimental support from E.R., A.S., M.S., G.L., and S.Z., as well as theoretical contributions from R.P.D., B.N., T.P.D., and A.F.K. The enhancement cavity–based HHG laser source system was conceived of by D.J.J. and A.D. and was developed by A.K.M. and D.J.J. All authors worked together to interpret and model the results and to write the paper. D.J.J. and A.D. were responsible for overall project direction, planning, and management. **Competing interests:** The authors have no competing interests. **Data and materials availability:** Data shown in the main text and supplementary materials are available at the Harvard Dataverse (*64*). All experimental data and calculations shown in the main text and in the supplementary materials are accessible at Zenodo (*65*).

SUPPLEMENTARY MATERIALS

23 November 2018; accepted 5 November 2019
10.1126/science.aaw1662

Direct determination of mode-projected electron-phonon coupling in the time domain

M. X. Na, A. K. Mills, F. Boschini, M. Michiardi, B. Nosarzewski, R. P. Day, E. Razzoli, A. Sheyerman, M. Schneider, G. Levy, S. Zhdanovich, T. P. Devereaux, A. F. Kemper, D. J. Jones and A. Damascelli

Science **366** (6470), 1231-1236.
DOI: 10.1126/science.aaw1662

A timely look into electron-phonon coupling

The coupling between electrons and phonons—lattice vibrations in solids—is responsible for macroscopic quantum phenomena such as superconductivity. Yet, experimentally measuring this coupling as a function of momentum and for a particular phonon mode is tricky. Na *et al.* used time- and angle-resolved photoemission spectroscopy to excite electrons in graphite and monitor their decay, which was accompanied by the release of phonons. The time constants of these decay processes provided direct information on electron-phonon couplings in this system.

Science, this issue p. 1231